communications chemistry

A Nature Portfolio journal

Article

https://doi.org/10.1038/s42004-025-01715-8

Probing the mechanism of phase transitions in halogen-substituted solvatomorph crystals of benzimidamides via thermal and chemical stimuli

Shubham Som[1], Somnath Dey[1], Peuli Ghosh[1], Anagha Ghosh[2], Swastik Mondal[2,3] & Deepak Chopra[1]

The screening of a molecule for its solid-state diversity is of importance in the chemical industry. The phenomena of phase transitions are also of interest as it allows one to understand the structural relationship that exists between the different crystal structures. This is expected to have implications in the observed properties in the substance of interest. With this background, the current study identifies two distinct phase transition phenomena in single crystals of 2-chloro-N'-(2-chlorophenyl) benzimidamide (**A**) and 2-bromo-N'-(2-bromophenyl)benzimidamide (**B**). Crystallization in DMSO produced solvatomorphs **AIIα** and **BII** at room temperature, while acetone and methanol yielded polymorphs **AI** and **BI**. The enantiotropic transition was characterized as an order-disorder phase transition in DMSO solvent, which resulted in conversion of **AIIα** to **AIIβ**, and was observed at Tc~199 K through variable-temperature SCXRD and low-temperature DSC. Since the solvent molecule ordering drives the phase transition, halogen-substituted benzimidamide interactions remain largely unchanged. However, immersing crystals of **AIIα** and **BII** in silicone oil triggered conversion to **AI** and **BI** crystals, completing the transition within 24 h, as confirmed by SCXRD studies. Thermal analysis techniques were employed to further investigate these transitions. Additionally, an in-depth examination of molecular packing was carried out to understand the underlying mechanism of the observed phase transition in these molecular crystals.

Phase transitions in molecular crystals are an important phenomenon and are driven by solvent and temperature, and thus provide powerful tools for tailoring the physical and chemical characteristics of solid-state materials. These transitions can influence crystal packing, polymorphism[1], and intermolecular interactions[2,3], thereby modifying properties such as solubility, optical behavior, and mechanical strength. Solvent-induced transformations often involve the incorporation or removal of solvent molecules, leading to solvated or desolvated crystal forms with unique structural features. Conversely, temperature-driven transitions can trigger reversible or irreversible changes in molecular conformation or crystal symmetry, as well as other physical properties[4,5]. These responsive behaviors are particularly advantageous in the development of smart materials, pharmaceuticals, and molecular electronics, wherein control over the solid-state attributes is crucial. Strategically harnessing these phase transitions allows for the customized tuning of thermal, electrical, mechanical, and optoelectronic properties to meet specific application demands[6–13].

Solid-state phase transitions can be broadly categorized by two mechanisms: nucleation and growth mechanism[14] and martensitic transitions[15–17]. Nucleation and growth transitions occur at a specific site and propagate throughout the crystal molecule by molecule. In contrast, martensitic transition involves a cooperative structure transformation, transitioning from the parent (austenite) phase to the daughter (martensite) phase. This process preserves the morphology of the crystal and establishes a well-defined orientational relationship between phases. Such transitions enable reversible single-crystal to single-crystal (SCSC) transformation, often characterized by abrupt structural changes[18–23]. Mechanisms underlying martensitic transitions include molecular gliding[24], rotations[12,25], and conformational changes[26], with amphidynamic[27,28] crystals being a notable

[1]Department of Chemistry, Indian Institute of Science Education and Research Bhopal, Bhopal, India. [2]CSIR-Central Glass and Ceramic Research Institute, Kolkata, India. [3]Academy of Scientific and Innovative Research (AcSIR), CSIR–Human Resource Development Centre, (CSIR–HRDC) Campus, Ghaziabad, India. e-mail: dchopra@iiserb.ac.in

subset. These crystals demonstrate rotational molecular motion within a rigid framework but are generally unable to exhibit the thermosalient effect due to restricted dynamics. SCSC phase transition can lead to the formation of domain structures, and relations between domains may be described by the lost crystallographic symmetry of the parent structure[29–32].

Solvent disorder can manifest in two primary forms: static and dynamic, and in rare cases, may be induced by a phase transition (PT). Differentiating between these two types is particularly challenging due to their overlapping characteristics. Static solvent disorder arises when molecules consistently occupy the same lattice positions across unit cells but exist in different, isolated configurations or orientations, distributed statistically[33]. In contrast, dynamic disorder is associated with molecular motion within the crystal and is marked by substantial atomic displacements[34]. Understanding the nature of solvent disorder is essential for interpreting structural data and predicting material behavior under varying conditions.

Several synthesized fluorinated benzimidamides exhibit notable differences. For instance, (*Z*)-4-fluoro-*N*′-(3-fluorophenyl)benzimidamide displays solvatomorphism in its solid state[35]. Another distinctive behavior was observed in the two polymorphic forms of (*Z*)-2-fluoro-*N*′-phenylbenzamidamide, where nearly identical and energetically equivalent molecular arrangements lead to the phenomenon of 'quasi-isostructural polymorphism'[36]. These weak intermolecular interactions play a vital role in phase transition and have a profound impact on thermal expansion properties. A particularly intriguing phenomenon was observed in ethynyl-substituted *ortho/meta*-substituted benzamides when exposed to silicone oil (SO), triggering an unusual phase transition process through SO[37].

As part of our continuing investigation into the crystal chemistry of substituted benzimidamides, we have synthesized and characterized a series of halogen-substituted compounds. Extensive crystallization screens were conducted, and the results for 2-chloro-*N*′-(2-chlorophenyl)benzimidamide (**A**) and 2-bromo-*N*′-(2-bromophenyl)benzimidamide (**B**) are presented in Fig. 1. This study focuses on the existence of enantiotropic phase transitions (PT) observed in individual solvatomorph crystals. An enantiotropic PT originated on account of the presence of positional disorder exhibited by dimethyl sulfoxide (DMSO), a molecule, over two sites as the temperature decreases. At room temperature, the DMSO molecule can adopt two configurations, $DMSO_A$ and $DMSO_B$, relative to compound **A**. These configurations are related by a two-fold rotational symmetry along the axis of the DMSO molecule. A potential interconversion between two forms could occur if the DMSO were able to rotate freely by 180° within the crystal lattice. At low temperature, the disorder freezes into ordered conformations of the solvent DMSO. This ordering triggers a PT at $T_c \sim 199$ K, resulting in a transformation from monoclinic **AIIα** to triclinic **AIIβ**. This transformation is characterized by a symmetry reduction and the emergence of domain structures. Additionally, immersing the crystals of **AIIα** in silicone oil (SO) initiates a phase transition (PT) to **AI**, mirroring a similar transition observed from **BII** to **BI** in the isomorphic brominated counterpart. These transitions were further supported by BFDH[38] morphology analysis, which provided deeper insights into the structural processes driving these changes.

Results and discussion

A series of *ortho*, *meta*, and *para* derivatives of halogen-substituted (Cl and Br) benzimidamides was synthesized. The current study extensively discusses the solid-state diversity observed specifically in two compounds: 2-chloro-*N*′-(2-chlorophenyl)benzimidamide (**A**) and 2-bromo-*N*′-(2-bromophenyl)benzimidamide (**B**), both of which exhibit distinct phase transition phenomena. The synthesis of these compounds, as outlined in Scheme 1, was followed by characterization using ^{1}H-NMR spectroscopy (Supplementary Figs. 1, 2). The crystallization of **A** and **B** was carried out by using the slow evaporation method with various solvents. At a low temperature of 3 °C, crystallization in solvents such as diethyl ether (DEE), acetone, and methanol resulted in block and needle-like morphologies corresponding to **AI** and **BI** (Supplementary Table 1) forms, respectively. In contrast, employing the same method with DMSO as the solvent at ambient temperature (23 °C) led to the formation of block-like morphology, as mentioned, identified as polymorphic **AIIα** (Supplementary Fig. 3) and **BII** (Supplementary Fig. 4).

A comprehensive search of the Cambridge Structural Database[39] (CSD) version 2024.1.0 was carried out to identify crystal structures exhibiting positional disorder in the DMSO solvent, a common feature in organic molecular crystals. The search yielded a total of 2015 entries where DMSO displays positional disorder. Among these, only two cases were found in which the disorder of DMSO directly contributed to a PT within the crystal system[33,34].

Single-crystal X-ray diffraction analysis confirmed the polymorphic nature of **A** and **B**. Both compounds displayed solvatomorphism in DMSO, crystallizing in the monoclinic $P2_1/n$ space group at ambient temperature. **AIIα** and **BII** are isomorphous (Supplementary Tables 3, 4)[40]. To quantify their isostructural nature, commonly used methods such as the unit-cell similarity index (Π), PXRD similarity index, and analysis of the root-mean-square-deviation (RMSD) were applied. The calculated values were 0.0031, 0.975, and 0.268, respectively (Supplementary Table 5). Additionally, packing similarity analysis using *Xpac*[41,42] between **AIIα** and **BII** yielded a dissimilarity index (x) of 4.1, further confirming their isomorphous[43] nature (Supplementary Fig. 10). Thermogravimetric analysis (TGA) further validated the presence of DMSO solvent molecules in the crystal structure. Weight loss observed around 180 °C corresponds to DMSO content, measured at 25% for **AIIα** and 20% for **BII** (Supplementary Fig. 5). These experimental values closely matched the theoretical predictions, the values being 23% for **AIIα** and 18% for **BII** (Supplementary Table 2), indicating inclusion of DMSO in the crystal voids. Other polymorphic forms, **AI** and **BI**, crystallized in $P2_1/c$ and $C2/c$ space groups, respectively (Supplementary Tables 3, 4).

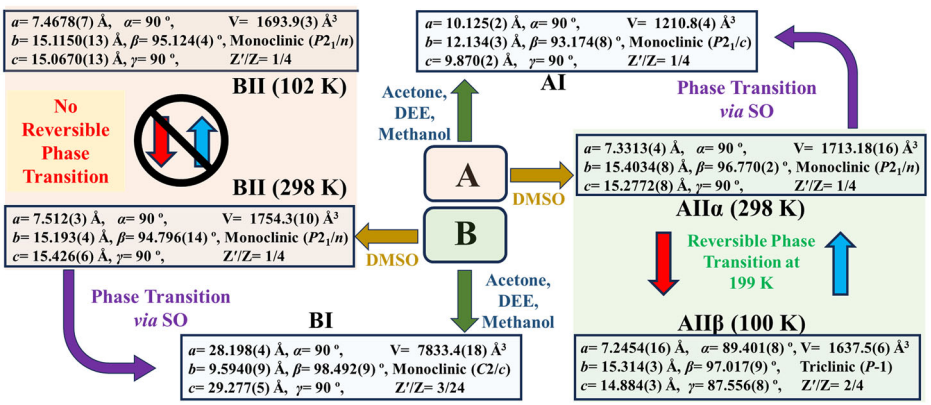

Fig. 1 | Phase transition in polymorphs of compounds A and B. Depiction of the formation of different phases and distinct phase transition phenomena via thermal and silicone oil (SO) in different polymorphs of compounds **A** and **B**.

Order-disorder thermal phase transition

Variable-temperature data collection reveals an order-disorder phase transition between **AIIα** and **AIIβ** (Supplementary Fig. 6). At 298 K, the **AIIα** crystallizes in the $P2_1/n$ space group with two molecules in the asymmetric unit ($Z' = 2$). The unit cell parameters at this temperature are $a = 7.3313(4)$Å, $b = 15.4034(8)$Å, $c = 15.2772(8)$Å, $\alpha = 90°$, $\beta = 96.770(2)°$, $\gamma = 90°$, V = 1713.18Å3 (Fig. 2a). Upon cooling to 100 K, the same crystal undergoes a significant structural transformation, characterized by marked destruction of the monoclinic symmetry and appearance of triclinic twin domains in the diffraction pattern (Fig. 2b) (Supplementary Fig. 12). At this low temperature (100 K), the **AIIβ** crystallizes in the *P*-1 space group, containing four molecules in the asymmetric unit. The corresponding unit cell parameters are $a = 7.2454(16)$Å, $b = 15.314(3)$Å, $c = 14.884(3)$Å, $\alpha = 89.401(8)°$, $\beta = 97.017(9)°$, $\gamma = 87.556(8)°$, V = 1637.5(6)Å3. The transition results in a modest percentage change in the unit cell dimensions $\Delta a = -1.17\%$, $\Delta b = -0.58\%$, $\Delta c = -2.57\%$, $\Delta \alpha = -0.67\%$, $\Delta \beta = 0.26\%$, $\Delta \gamma = -2.72\%$, $\Delta V = -4.59\%$. The distortion in the alpha (α) and gamma (γ) angles, measured at −0.67% and −2.27% respectively, highlights the structural difference between the **AIIα** and **AIIβ** phases. The observed twinning is pseudo-merohedral, characterized by a 180° rotation along the *b*-axis. Reflections from the twin domains are either partially resolved or overlapping. The twin law is represented by the matrix [−1 0 0; −0.188 1 −0.033; 0 0 −1]. SCXRD data at intermediate temperature (220 K) revealed the presence of only a single domain (green color), as depicted in Fig. 2a. After the PT, this single domain evolved into distinct twin domains (green and red color), labeled as domain 1 and domain 2, which are clearly illustrated in Fig. 2b.

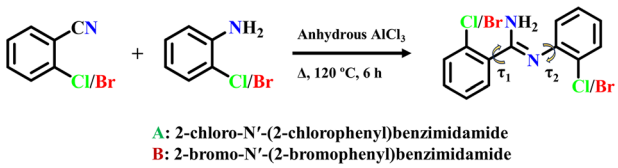

A: 2-chloro-N′-(2-chlorophenyl)benzimidamide
B: 2-bromo-N′-(2-bromophenyl)benzimidamide

Scheme 1 | Molecular design. General synthetic scheme for the synthesis of halogen-substituted benzimidamides, **A** and **B**.

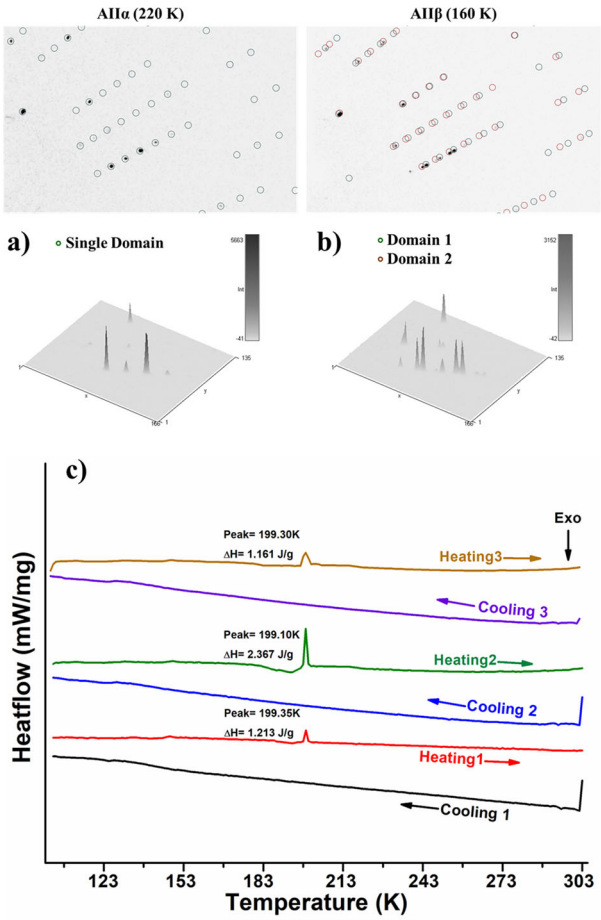

Fig. 2 | SCXRD and DSC analysis. a Reflection image at 220 K (single domain) in green circle and **b** 160 K (twinned domains) depicted in red and green circles. **c** Low-temperature DSC traces over three cooling-heating cycles, showing a consistent endothermic peak associated with the conversion of **AIIβ** to **AIIα** phase.

To confirm the SCSC phase transition and explore its thermodynamic properties, a low-temperature DSC measurement was conducted. During the first cooling-heating cycle, crystals of the **AIIα** phase were cooled from room temperature (298 K) to 120 K at a slow rate of 1 K min^{-1}. No distinct thermal event or phase transition was observed during cooling, indicating that the transformation from **AIIα** to the low-temperature **AIIβ** phase could not be detected under these conditions. Upon heating from the cooled state, a pronounced endothermic phase transition was detected at $T_{cycle\ 1} = 199.35$ K. This transition corresponds to the conversion of **AIIβ** back to **AIIα** phase, accompanied by an enthalpy change of 1.213 J g^{-1} (Fig. 2c). The continuation of the DSC experiments for the second and third cycles yielded highly consistent results. The transition temperature remained close to the initial value at $T_{cycle\ 2} = 199.10$ K and $T_{cycle\ 3} = 199.30$ K in the second and third cycles, while the associated enthalpy changes were 2.367 J g^{-1} and 1.161 J g^{-1}, respectively (Fig. 2c). Variable-temperature SCXRD measurements confirmed that the phase transition is fully reversible, with the formation of the parent phase **AIIα** after heating. This structural reversibility corroborates the DSC results, underscoring the stability of the crystalline lattice through repeated cooling-heating cycles.

To examine the changes in the molecular conformation in molecule **A** during the PT **AIIα ↔ AIIβ**, the crystal packing was analyzed using 20 neighboring molecules in each form. The results indicate that all the molecules remained invariant throughout the process of the PT of **AIIα ↔ AIIβ**. The unit-cell similarity index (Π), PXRD similarity index, and root-mean-square-deviations (RMSD) were calculated as 0.015, 0.987, and 0.251, respectively (Supplementary Table 6). Additionally, the *Xpac* analysis between **AIIα ↔ AIIβ** yielded a dissimilarity index (x) of 2.7 (Supplementary Fig. 11). Together, these parameters confirm the isostructural nature of both forms, indicating no significant changes in the crystal packing or conformation of molecule A during phase transition. Consequently, the overall structure remained rigid across the entire temperature range.

Interestingly, the relative population of DMSO in two configurations, I and II, varies with temperature, supporting the dynamic nature of the disorder-order. In the **AIIα** phase, between 298 and 200 K, the DMSO molecules exhibit disorder of their position, adopting two distinct configurations I and II, which are related by a 180° rotation (Fig. 3a). The crystal packing analysis confirms the presence of disordered DMSO molecules in the lattice within this temperature range. However, following the PT, the DMSO becomes fully ordered in the **AIIβ** phase (Fig. 3b).

Variable-temperature SCXRD reveals a gradual shift in the occupancy ratio (Fig. 3c) of the DMSO configurations from 0.818(2):0.182(2) at 298 K to 0.954(2):0.046(2) at 200 K. Therefore, the dynamic disorder has already significantly decreased in **AIIα** before progressing toward the completely ordered twinned triclinic **AIIβ** phase. This explains why no detectable exothermic peak corresponding to the **AIIα** to **AIIβ** transformation was observed in the DSC during cooling. The gradual ordering of the DMSO molecules, combined with the small enthalpy change, further accounts for the absence of an exothermic peak in the DSC curves during repeated cycles. On the other hand, during heating, the crystal transforms from a completely ordered **AIIβ** to a disordered **AIIα** structure, showing the sharp cooperative nature of the transition marked by the endotherm during consecutive cycles. This fully reversible behavior, with consistent occupancy values across cycles, *highlights a rare and novel reversible order-disorder transition involving changes in the orientation of the DMSO solvent*. These

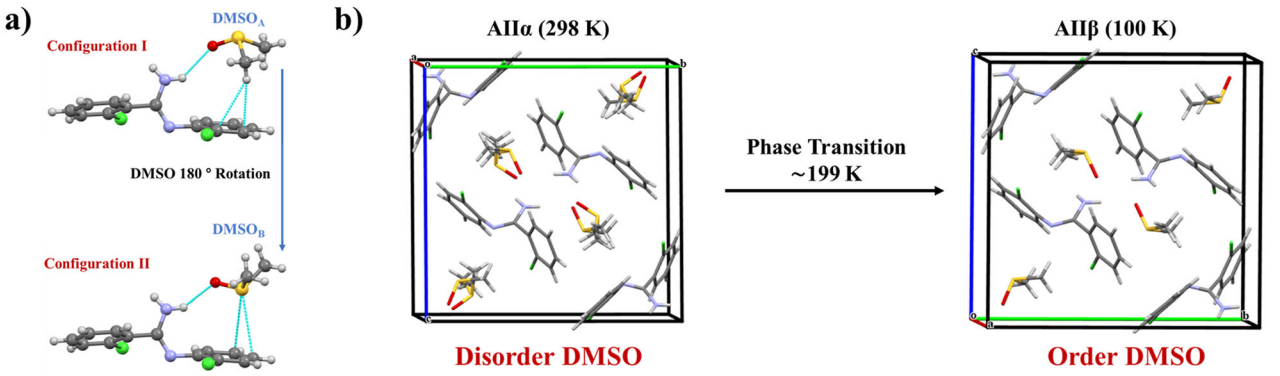

c)

DMSO Occupancy/ Temp (K)	298	280	260	240	220	200	Phase Transition	160	100	160	Phase Transition	200	220	240	260	280	298
	AIIα (Monoclinic Form)							AIIβ (Triclinic Form)				AIIα (Monoclinic Form)					
$DMSO_A$	0.818(2)	0.847(2)	0.877(2)	0.905(2)	0.932(2)	0.954(2)		Order DMSO				0.953(2)	0.931(2)	0.905(2)	0.875(2)	0.843(2)	0.813(2)
$DMSO_B$	0.182(2)	0.153(2)	0.123(2)	0.095(2)	0.068(2)	0.046(2)						0.047(2)	0.069(2)	0.095(2)	0.125(2)	0.157(2)	0.187(2)

Fig. 3 | Configurational behavior of DMSO at variable temperature. a Two distinct configurations (I and II) of the DMSO solvent. **b** Disorder to order transformation involving the DMSO molecule. **c** Temperature-dependent occupancy of DMSO, measured from 298 K to 100 K and back to 298 K in **AIIα**.

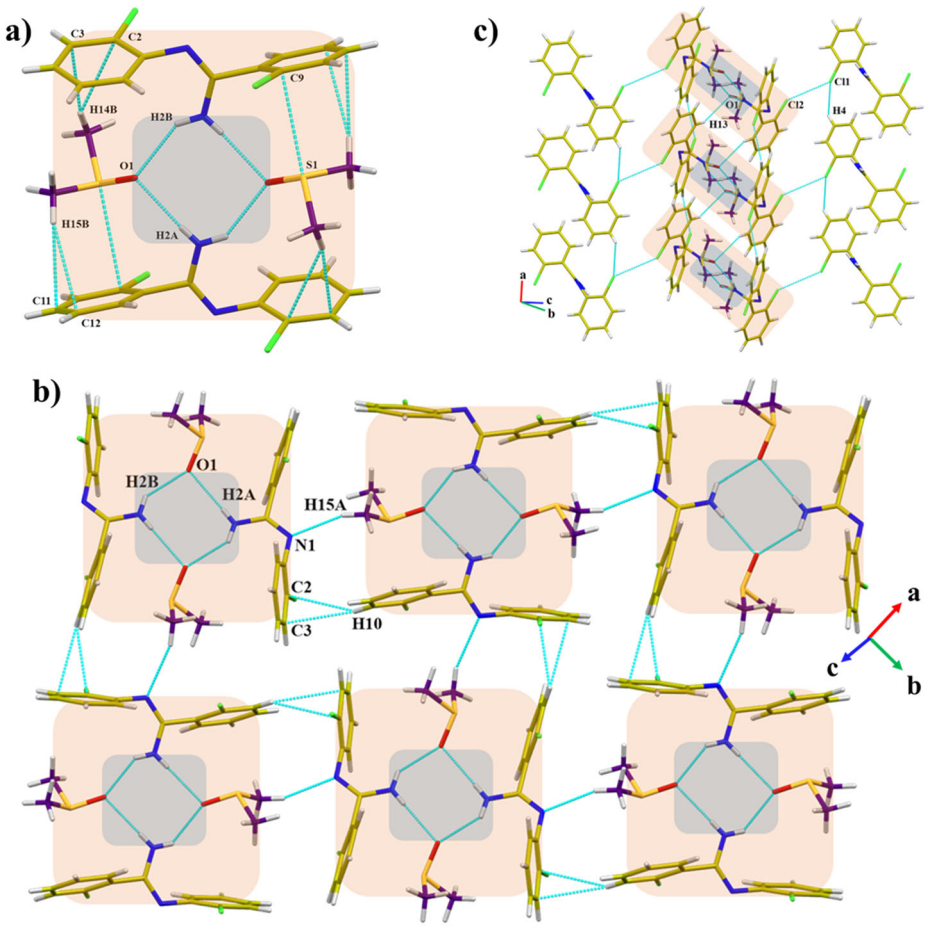

Fig. 4 | Crystal packing arrangement of AIIα. **a** *Tetramer* formation via N-H…O, C-H…π and S…π interactions, **b** crystal packing along *ab*-plane and, **c** *ac*-plane in **AIIα**, respectively.

findings confirm that the PT between **AIIα** ↔ **AIIβ** is fundamentally driven by an order-disorder transformation exclusively of the DMSO solvent molecules embedded in the crystal lattice. The driving force for the order-disorder PT is due to the increase in configurational entropy, whose magnitude is Rln2 = 5.76 J mol^{-1} K^{-1}[33,44–46].

Crystal structure analysis of AIIα↔AIIβ and BII

The analysis of the crystal structure of **AIIα** using SCXRD confirmed the presence of a supramolecular assembly comprising **A** and **DMSO** in a 1:1 ratio. This assembly is stabilized by a strong N2-H2A…O1 hydrogen bond. The crystal structure displays the formation of a stronger tetrameric motif

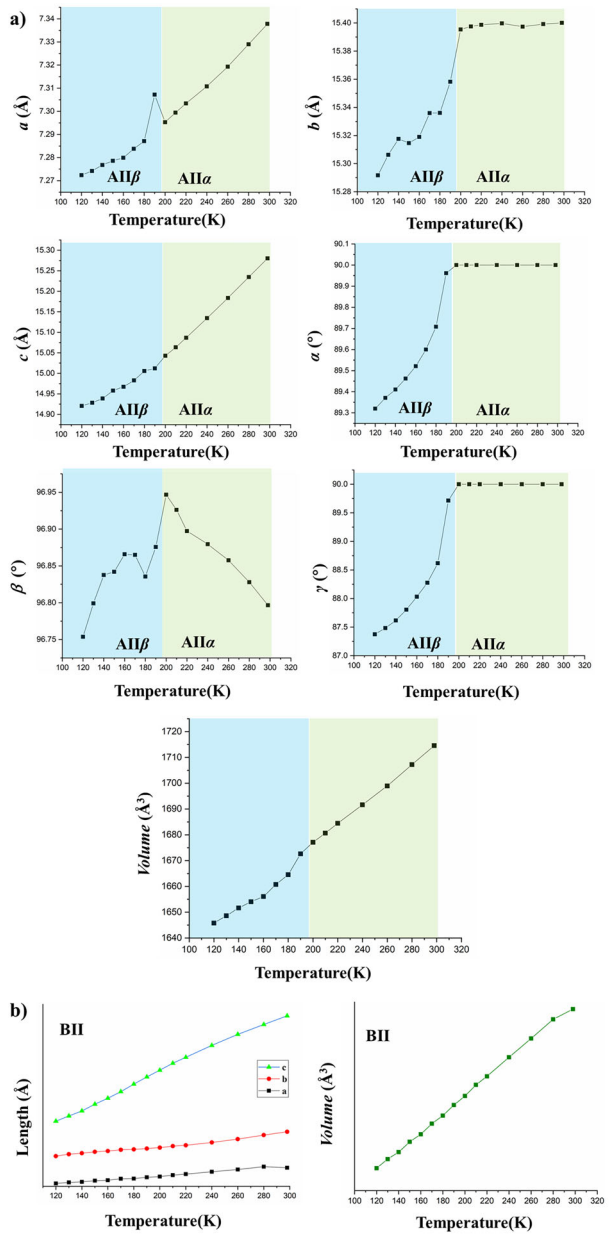

Fig. 5 | Variable-temperature SCXRD. a Variation of unit cell characteristics (*a, b, c, α, β, γ*) and unit cell volume during the PT from **AIIα** to **AIIβ**, cyan and lime colors represent the two different phases **AIIβ** and **AIIα**, respectively. **b** Change in unit cell length and volume in **BII**. The data points correspond to the cooling of the crystal from RT to 100 K.

(Fig. 4a), stabilized by a network of intermolecular interactions, including N2-H2B…O1, S1…C9(π), and C14-H14C… C3(π) interactions. These tetramers are arranged in an alternative manner along the *bc*-plane, connected through C10-H10…C9(π)/C10(π) interactions (Fig. 4b). Furthermore, the two-dimensional sheets formed are aligned in parallel, stabilized by additional C4-H4…Cl1, Cl1…Cl2, and C13-H13…O1 interactions along the *ab*-plane (Fig. 4c).

For **AIIβ**, SCXRD analysis revealed four distinct molecules of **A** in the asymmetric unit, along with DMSO in a 2:2 ratio. C13-H13…O1, C29-H29B…N1, C30-H30B…N1 and C28-H28B…N3 interactions stabilized the asymmetric unit. Similar to **AIIα**, tetramers (Supplementary Fig. 13a) are formed through N2-H4A…O2, N2-H4B…O2 hydrogen bonds and additionally supported by S1…C9, S2…C22, and C23-H23…C2(π)/C3(π) interactions, enhancing structural stability. These tetramers are organized into 2-D sheets exhibiting an alternative structure along the *bc*-plane (Supplementary Fig. 13b). Successive sheets are interconnected by well-oriented C26-H26…O2 contacts, along with synergistic interactions, like Cl1…Cl4, and Cl2…Cl3 further reinforces the crystal packing along the *ab*-plane (Supplementary Fig. 13c). Their respective energy framework analyses are presented in (Supplementary Fig. 14) with the corresponding outputs shown in (Supplementary Figs. 15, 16), and the interaction details provided in (Supplementary Tables 9, 10).

The **B** polymorph, especially **BII**, exhibits solvatomorph characteristics. At 298 K, SCXRD analysis confirmed the presence of a two-component system comprising **B** and the solvent DMSO. The form crystallizes in the $P2_1/n$ space group with two molecules in the asymmetric unit (Supplementary Fig. 7). These molecules are connected through a robust hydrogen-bond network dominated by N2-H2B…O1 interactions. The DMSO solvent molecules are fully disordered, with an occupancy ratio of **0.683(3):0.317(3)**. Variable-temperature data collection indicates that no phase transition was observed during the temperature variation from 298 to 100 K. Strong intermolecular interactions, including N2-H2A…O1, C10-H10…C2(π)/C3(π), and S1…C9(π), lead to the formation of a tetrameric motif in both polymorphs due to their shared isomorphous characteristics. These tetramers are organized into a herringbone arrangement along the (101) plane, stabilized by C14-H14B…N1, and C15-H15C…C2 interactions. Furthermore, the 2D sheets formed in the structure are interconnected through C13-H13…O1, C4-H4…Br1, and Br1…Br2 interactions (Supplementary Fig. 17). Their respective energy framework analyses are presented in (Supplementary Fig. 18) with the corresponding outputs shown in (Supplementary Figs. 19, 20), and the interaction details provided in (Supplementary Table 11).

Variable-temperature SCXRD

To examine the PT behavior at various temperatures, ϕ-scan data was collected over a temperature range from 298 K to 120 K. Initially, a 20 K decrement was applied during the transition from 298 to 220 K, followed by 10 K intervals between 220 and 120 K. Temperature-dependent variations in the lattice parameters and unit cell volume were observed for two distinct phases involved in the **AIIβ**-**AIIα** transition (Supplementary Table 7). Notable shifts in the lattice parameters (*a*, *b*, *c*) and unit cell angles (*α*, *β*, *γ*) and volume in the vicinity of ~190 K clearly indicate a PT (Fig. 5a). Each parameter displayed either a visible discontinuity or a marked change in slope near this temperature. The observed fluctuation at 190 K occurs near the phase transition temperature and likely reflects the formation of twin domains. As a result, the unit cell parameters at this temperature may be less reliable compared to those obtained at other temperature ranges. The blue shaded region represented the **AIIβ phase**, while the green area denoted **AIIα**, underscoring a subtle, yet significant structural transformation between the two phases.

In contrast, the **BII** crystal exhibited a steady, linear change in the unit cell parameters across the same temperature range (Supplementary Table 8), indicating the absence of any PT (Fig. 5b).

To further investigate the presence and absence of low-temperature order-disorder PT behavior between the isomorphous crystal structures **AIIα** and **BII**, the temperature-dependent changes in the geometrical features of various intermolecular interactions were analyzed. Crystal packing analysis suggests that the differing SCSC phase transition behavior between **AIIα** ↔ **AIIβ** is primarily influenced by Cl…Cl interactions, which occur specifically along the crystallographic [103] direction. While the rigid hydrogen-bonded tetramers remain consistent across both forms, the key distinction lies in the nature of halogen-halogen contacts.

At 298 K, these weak intermolecular Cl…Cl interactions span a distance of 3.627 Å, which exceeds the sum of the vdW radii (Fig. 6a). As the temperature decreases to 200 K, the distance contracts to 3.551 Å (Fig. 6b), and after the phase transition at 100 K, it further shortens to 3.437 Å (Fig. 6c). This structural adaptability creates sufficient space for the DMSO solvent to adopt an ordered conformation in the crystal structure below the phase transition temperature.

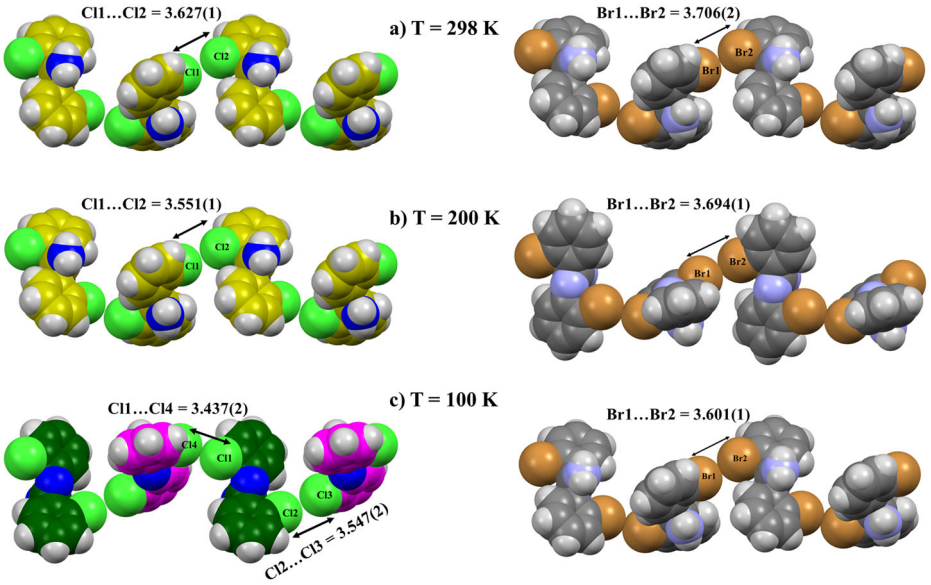

Fig. 6 | Effect of temperature on intermolecular interactions. Variation of geometrical parameters of halogen-halogen interactions at different temperatures **a**) 298 K, **b**) 200 K, and **c**) 100 K in **AIIα** and **BII**.

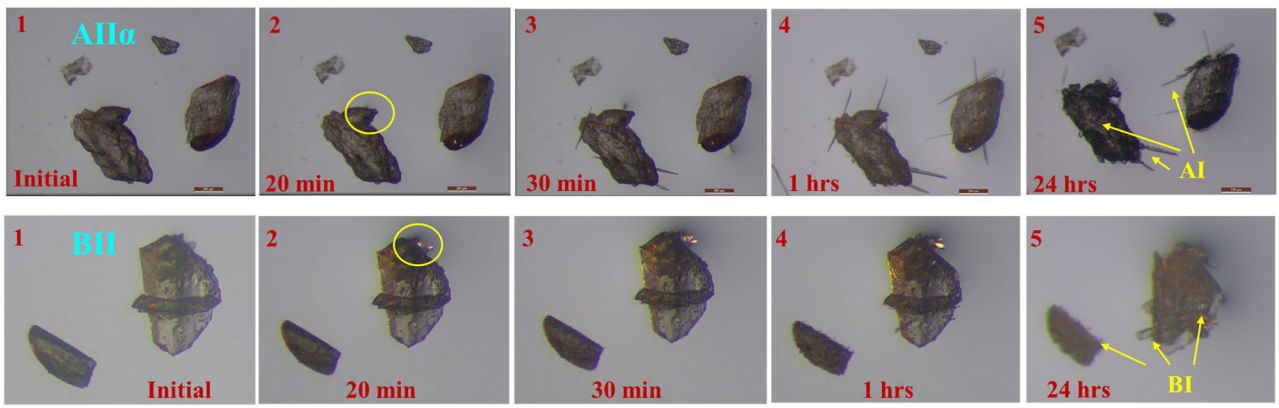

Fig. 7 | Optical visualization in crystals. Optical images of the parent crystals (**AIIα** and **BII**) and appearance of daughter phase (**AI** and **BI**), respectively, as depicted in a yellow circle, and the complete formation after 24 h.

In contrast, the **BII** crystalline phase features shorter Br…Br interactions. At 298 K, the Br…Br distance is 3.706 Å (Fig. 6a), which is nearly equal to twice the vdW radii. This distance decreases to 3.649 Å (Fig. 6b) at 200 K and further reduces to 3.601 Å (Fig. 6c) near 100 K. Although variable-temperature studies reveal a gradual change in the order-disorder behavior of DMSO between 298 K to 200 K, no further change is observed below 200 K, as this transition becomes limited and eventually halts due to steric constraints. The continued presence of DMSO disorder at lower temperature (down to 100 K) in **BII** is attributed to the absence of sufficient free volume, which prevents complete reordering of the solvent molecules. Additionally, Saha et al. and Nangia et al. studies indicate that Br…Br interactions are less responsive to temperature change and exhibit lower thermal expansion (TE) behavior, whereas Cl…Cl interactions are more temperature sensitive and display more pronounced TE characteristics[47,48].

Phase transition in silicone oil

An intriguing SCSC phase transition was observed in the presence of silicone oil (SO). During the process of mounting crystals for SCXRD experiments, anomalous behavior was detected in the crystals of **AIIα** and **BII** when immersed in SO. The first signs of the phase transition appeared during the mounting of crystals for single-crystal data collection, where SO is commonly employed as a cryogenic oil for crystal mounting. Needle-like crystals began to emerge from the block crystals of **AIIα** and **BII**, indicating a rapid transformation (Fig. 7). This dynamic change occurred swiftly, with multiple crystals of similar shapes forming during the process.

A comparable anomalous transformation was also observed in the laboratory, where the addition of a small drop of SO induced the conversion of the crystals into another form. However, attempts to replicate these findings using other hydrophobic polymers were unsuccessful, highlighting the unique role of SO in this phenomenon.

To explore polymorphic interconversion at room temperature, temporal microscopic imaging and thermal characterization were employed to assess the stability profile of the crystals. When block crystals were submerged in SO, the growth of needle-like crystals began within 20 min, and this transformation continued until complete conversion into the second form occurred after 24 h. SCXRD analysis of the newly formed needle-shaped crystals confirmed the generation of **AI** and **BI** polymorphs (Fig. 7).

The thermal stability of the polymorphs was assessed using differential scanning calorimetry (DSC), thermogravimetric analysis (TGA), and hot stage microscopy (HSM). The synthesized crude compound, referred to as the bulk compound, is denoted as compound (A) and compound (B), corresponding to their respective representation in Scheme 1. The DSC thermograms, presented in color-coded format, for the bulk compound (**A**) are represented in black, polymorph **AI** in blue, and polymorph **AIIα** in red (Fig. 8a). The DSC curve for the bulk compound (**A**) displays a single endothermic peak at 105 °C, with an associated enthalpy change (ΔH) of

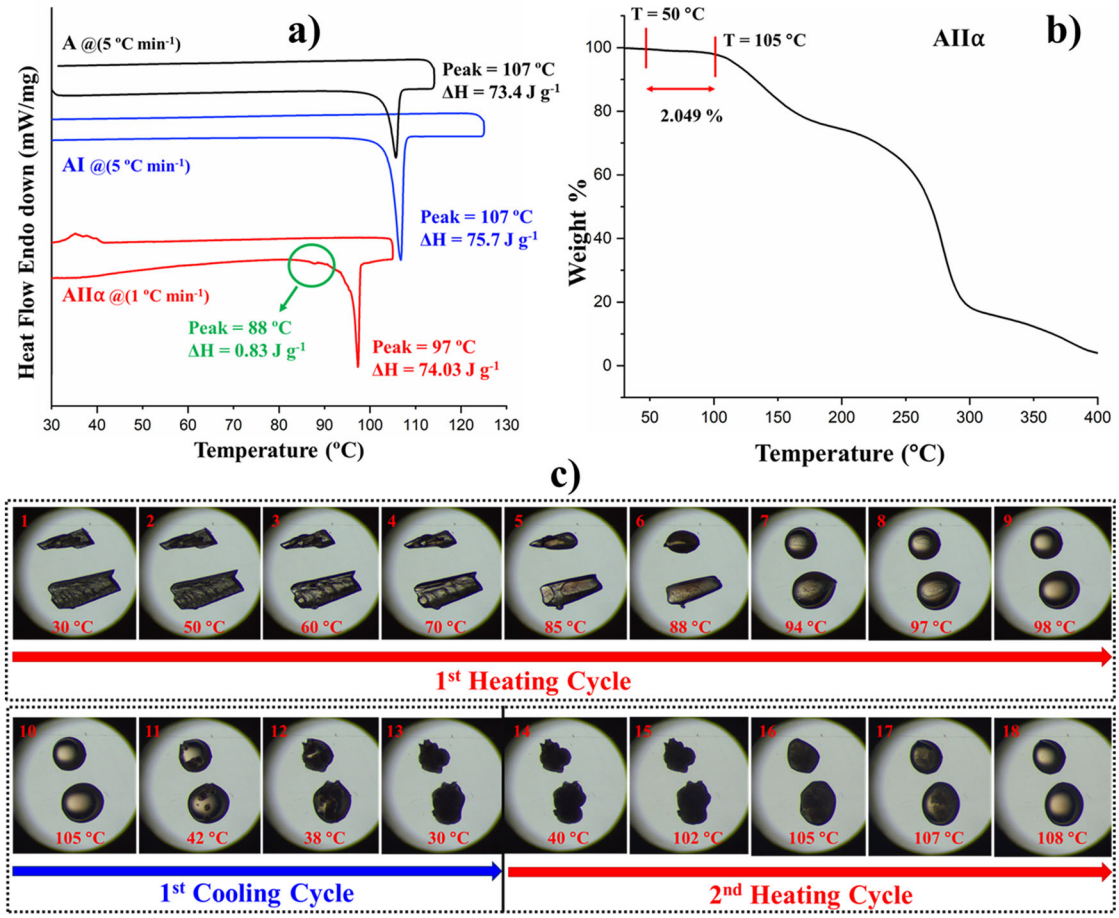

Fig. 8 | Thermal analysis in AIIα and its polymorphs. a The DSC plot of the bulk material and its polymorphic phases (**AI** and **AIIα**) shows endothermic peaks, highlighted by a green circle, specifically in **AIIα**. **b** DSC plot showing the continuation of the thermal processes for 2nd and 3rd cycles in **AIIα**. **c** TGA analysis of **AIIα** indicates the corresponding weight loss. **d** HSM images capture the thermal events associated with the **AIIα** crystal in different heating and cooling cycles.

73.4 J g^{-1} (Fig. 8a). Similarly, polymorph **AI** (blue) exhibits comparable melting behavior, displaying an endothermic peak at 104 °C with ΔH = 75.7 J g^{-1} (Fig. 8a).

In contrast, polymorph **AIIα** (red) exhibits a more complex thermal profile. The DSC trace begins with a broad endothermic peak starting around 50 °C, followed by a minor endothermic peak at 88 °C (ΔH = 0.83 J g^{-1}), highlighted by a green circle, and then a major melting peak at 96 °C (ΔH = 74.03 J g^{-1}) (Fig. 8a). Upon cooling, a broad exothermic peak appears around 40 °C. During subsequent DSC heating and cooling cycles (2nd and 3rd), the curves show an anomalous broadening with several endothermic thermal events starting near 85 °C, eventually culminating in a final peak at 106 °C that closely resembles the melting behavior of polymorph **AI** (Fig. 8b). This pattern suggests the formation of multiphases, which is likely due to the presence of residual DMSO solvent, which causes components to melt across a range of temperatures in repeated DSC cycles. TGA analysis supports this interpretation, indicating a 2.049% weight loss, corresponding to the loss of DMSO solvent, between a temperature range of 50 °C to 105 °C (Fig. 8c).

Further insights into this behavior were obtained through HSM. Images captured during heating show the pristine **AIIα** crystals (image 1 in Fig. 8d) begin to undergo desolvation of DMSO solvent after 50 °C (image 2 in Fig. 8d). As the temperature rises, desolvation increases slowly, leading to the emergence of an unidentified phase, following minor solvent loss (image 3–6 in Fig. 8d). This unknown phase melts at 96 °C, which is coincident with the major peak in the DSC endotherm (image 7–9 in Fig. 8d). Upon cooling, solidification occurs at ~40 °C (image 11–13 in Fig. 8d). In the second HSM cycle, the newly formed phase remains visually stable at lower temperatures (image 14 in Fig. 8d), and no significant changes are observed until it melts at 106 °C (image 15–18 in Fig. 8d), a behavior that closely mirrors polymorph **AI**, as indicated by the second DSC cycle. The variable-temperature SCXRD data were sufficient to confirm that the **AIIα** crystal exhibited multiple domains at an elevated temperature of 362 K. Upon thermal treatment, these domains transitioned into a second polymorphic form, corresponding to **AI** (Supplementary Fig. 26).

Overall, the combined thermal analysis (DSC, TGA, HSM, and SCXRD) reveals that polymorphs **AI** and **AIIα** possess distinct thermal behaviors. Polymorph **AI** exhibits a sharp melting point, indicative of its thermodynamic stability, corresponding to bulk form **A**. In contrast, **AIIα** displays a more complex and multiphase thermal response due to residual DMSO, which initiates desolvation upon heating and facilitates the transformation into an intermediate phase that ultimately resembles **AI**. These findings are supported by TGA data indicating solvent loss and HSM observations of phase transitions. PXRD analysis further confirms **AI** as the dominant crystalline form (Supplementary Fig. 8). Collectively, the results identify polymorph **AI** as the most thermodynamically stable form with higher lattice energy compared to polymorph **AIIα** (Supplementary Table 15).

For the bulk compound **B**, DSC analysis reveals an endothermic peak at 114 °C with an associated enthalpy change (ΔH) of 55.9 J g^{-1} (Fig. 9a). Polymorph **BI** (blue) shows a similar thermal behavior, exhibiting a sharp endothermic peak at 114 °C (ΔH = 55.9 J g^{-1}), as illustrated in Fig. 9a. Meanwhile, the isomorphous polymorph **BII** (red) exhibits a DSC profile

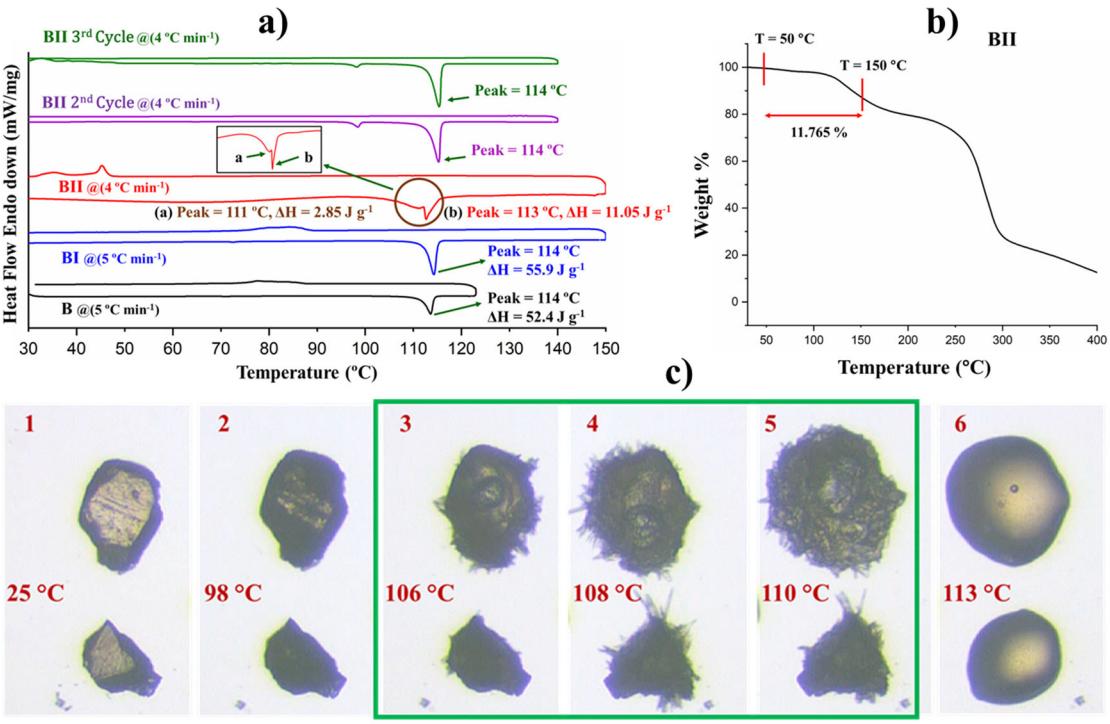

Fig. 9 | Thermal analysis in BII and its polymorphs. a The DSC plot of the bulk material and its polymorphic phases (**BI** and **BII**), respectively, shows endothermic peaks highlighted by brown circles, in **BII** crystals. **b** TGA analysis of **BII** displays the corresponding weight loss. **c** HSM images illustrate the thermal events observed in the **BII** crystals.

resembling that of **AIIα**, beginning with a broad endothermic region at 70 °C, followed by a minor endothermic peak (**a**) at 111 °C (marked with a brown circle) ($\Delta H = 55.9\ J\ g^{-1}$), and a major melting peak (**b**) at 114 °C ($\Delta H = 11.05\ J\ g^{-1}$), corresponding to the melting point of **BI** (Fig. 9a).

TGA analysis confirms that **BII** initially contains 20.004% DMSO solvent. By 150 °C, approximately 11.765% of this content is lost, indicating that some solvent remains during the cooling cycle (Fig. 9b). In subsequent DSC runs (2nd and 3rd cycles), the melting peak at 114 °C consistently reappears, suggesting the formation and stability of polymorph **BI** (Fig. 9a). HSM observations support this conclusion, desolvation begins as the temperature rises (Fig. 9c), followed by nucleation and growth of **BI** crystals around 108 °C, highlighted in a green box (Fig. 9c), which melt at 114 °C, consistent with DSC findings. This observation was further supported by variable-temperature SCXRD data, which showed that the **BII** crystals transformed into multiple domains at 383 K. Upon thermal treatment, these domains transitioned into a second polymorphic form, corresponding to **BI** (Supplementary Fig. 27).

The thermal analysis confirms that polymorph **BI** represents the thermodynamically stable form of compound **B**. Starting from form **BII**, it undergoes partial desolvation and subsequent transformation into **BI** upon heating, thereby indicating conversion into the thermodynamically more stable form **BI** (Supplementary Table 15). The consistent endothermic peak at 114 °C across multiple DSC cycles, supported by TGA, HSM, and PXRD data (Supplementary Fig. 8), highlights the reproducibility in the formation of **BI** on account of its greater stability.

Crystal packing analysis

To achieve the observed polymorphic transition, a comparative structural analysis must be conducted. The 3D arrangement in polymorphic forms varies due to the presence of DMSO solvent molecules in **AIIα** and **BII**, which contrasts with the solvent-free forms **AI** and **BI**. The crystal packing of **AIIα** (Fig. 4) and **BII** (Supplementary Fig. 17) has been previously discussed. SCXRD analysis reveals that **AI** crystallized in the centrosymmetric monoclinic space group $P2_1/c$, with one molecule in the asymmetric unit. Its structure is characterized by strong hydrogen bonding N-H…N and π… π stacking interactions (Fig. 10a). These interactions result in alternating molecular arrangements along the *c*-axis, forming 2D sheets that further dimerize through C-H…Cl contacts along the *a*-axis, creating an extended network in the *ab*-plane (Supplementary Fig. 20a).

In contrast, **BI** crystallizes in the monoclinic space group *C*2/*c*, with three molecules in the asymmetric unit. The structure of **BI** features robust N-H…N interactions that facilitate the formation of molecular chains (Fig. 10b). Additionally, interactions, such as C-H…Br and Br… π contacts contribute to the formation of a two-dimensional sheet, culminating in a wavelike molecular arrangement in the *bc*-plane (Supplementary Fig. 20b).

At the molecular level, the supramolecular architecture of these polymorphs was further analyzed by quantifying the stabilization energies of key interaction motifs. The **AIIα** and **BII** polymorphs are isostructural and incorporate DMSO molecules, resulting in similar crystal packing. Both structures exhibit N-H…N tetramer motifs, with stabilization energies of $-39.7\ kJ\ mol^{-1}$ and $-43.5\ kJ\ mol^{-1}$ for **AIIα** (Supplementary Fig. 14) and $-38.5\ kJ\ mol^{-1}$ and $-46\ kJ\ mol^{-1}$ for **BII** (Supplementary Fig. 18). These tetramers are further stabilized through C-H…N interactions with DMSO, contributing $-26.9\ kJ\ mol^{-1}$ and $-28.5\ kJ\ mol^{-1}$, respectively. Additionally, C-H…O interactions provide further stabilization, measured at $-18.5\ kJ\ mol^{-1}$ and $-16.2\ kJ\ mol^{-1}$, respectively. These interactions emphasize the central role of the DMSO solvent in the overall structural integrity.

On the other hand, the **AI** and **BI** polymorphs, which do not contain solvent molecules, exhibit stronger N-H…N interactions with stabilization energy of $-55.3\ kJ\ mol^{-1}$ for **AI** (Supplementary Fig. 21) and ($-52.4\ kJ\ mol^{-1}$, $-59\ kJ\ mol^{-1}$) for **BI** (Supplementary Fig. 22). In **AI**, C-H…Cl and π… π interactions, and in **BI** C-H…Br contacts further reinforce the 3D network. Lattice energy calculations also indicate that **AI** and **BI** possess greater stabilization compared to the DMSO-containing counterpart, **AIIα** and **BII** (Supplementary Table 15). The energetics comparison confirms the relative thermodynamic stability of the solvent-free polymorphs.

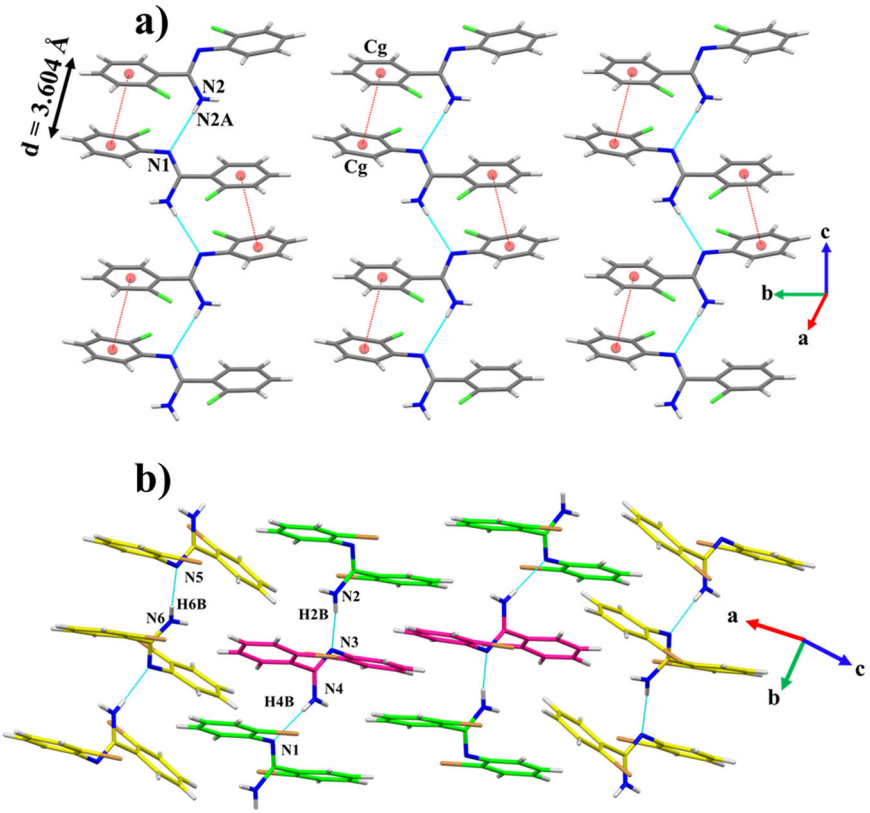

Fig. 10 | Crystal packing. a Crystal packing illustrating N-H…N intermolecular interactions in **AI**, and **b BI** viewed along the *bc*-plane.

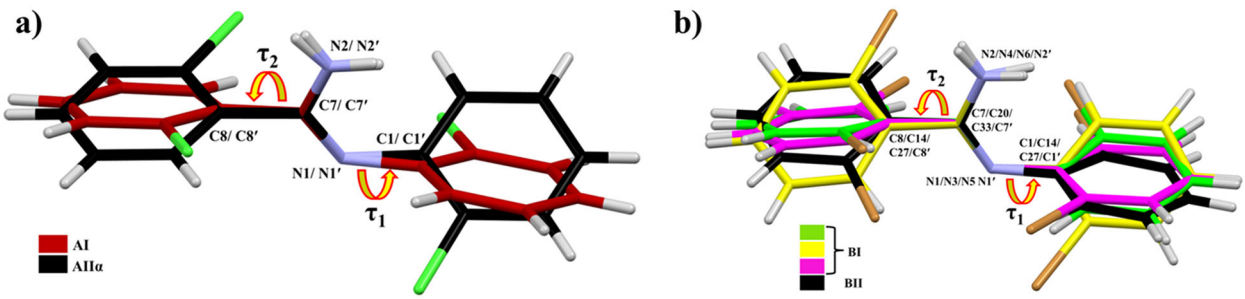

Fig. 11 | Structure overlay. Molecular conformation along τ_1 and τ_2 with structure overlay in **a AI** and **AIIα, b BI** and **BII**.

Upon exposure to external stimuli, such as heat or SO, the **AIIα** and **BII** crystals undergo solvent loss (DMSO), which induces a reorganization into energetically more favorable supramolecular motifs, thereby transitioning into **AI** and **BI**. These transformations highlight the structural distinctions between the polymorphs **AIIα** and **BII** are binary systems incorporating solvent, whereas **AI** and **BI** are single-component structures.

A structural overlay analysis using Mercury software supports these findings, showing a root-mean-square (RMS) of 0.0116 for the **A** polymorph system (Fig. 11a) and 0.0143 for the **B** polymorphic system (Fig. 11b), further confirming the close structural relationship and subtle difference among these forms.

Preliminary comparative findings revealed that the crystal structure of **AIIα** and **BII** remains stable at room temperature due to their favorable supramolecular motifs. However, when exposed to SO, a phase transition to the second polymorph is initiated, producing needle-shaped crystals on the surface of the parent crystals. Face indexing of both crystals was performed using D8-Quest, and the resulting images have been provided in Supplementary Fig. 24. For **AIIα** polymorph, the identified crystal faces were (011), (01-1), (100), and (001), while for **BII**, the observed faces were (101), (011), (-10-1), and (-111) (Supplementary Fig. 25). These experimental results supported the results obtained from the prediction via BFDH morphology analysis. To reinforce the analysis of crystal surface characteristics, we also calculate the percentage area of each facet for both **AIIα** and **BII** crystals using Materials Studio[49,50]. The dominant facet for both forms was (011), accounting for approximately 84% of the total surface area in **AIIα** (Supplementary Fig. 27) and 82% in **BII** (Supplementary Fig. 28), as detailed in Supplementary Table 14. Additionally, the calculated attachment energy (E_{att}) was lowest for the (011) facet, measuring −51.64 kJ mol^{-1} for **AIIα** and −53.74 kJ mol^{-1} for **BII**, compared to other facets (Supplementary Table 14).

It may be postulated that this transformation is driven by possible supramolecular interactions, involving the oxygen atom in DMSO and the hydrophobic chlorophenyl/bromophenyl moiety in compound A/B with the silicon atoms in silicone oil (Fig. 12a, b), *which may facilitate the elimination of DMSO solvent and the conversion of the resulting solid into more stable forms, namely **AI** and **BI**, respectively*. The interaction with SO begins at the crystal surface, wherein the progression of the **AI**/**BI** phase boundary on the surface of crystals of **AIIα**/**BII** is clearly visible in optical images (Fig. 7). The spatial configuration and properties of the crystal surface are crucial in dictating the SO-induced phase transition.

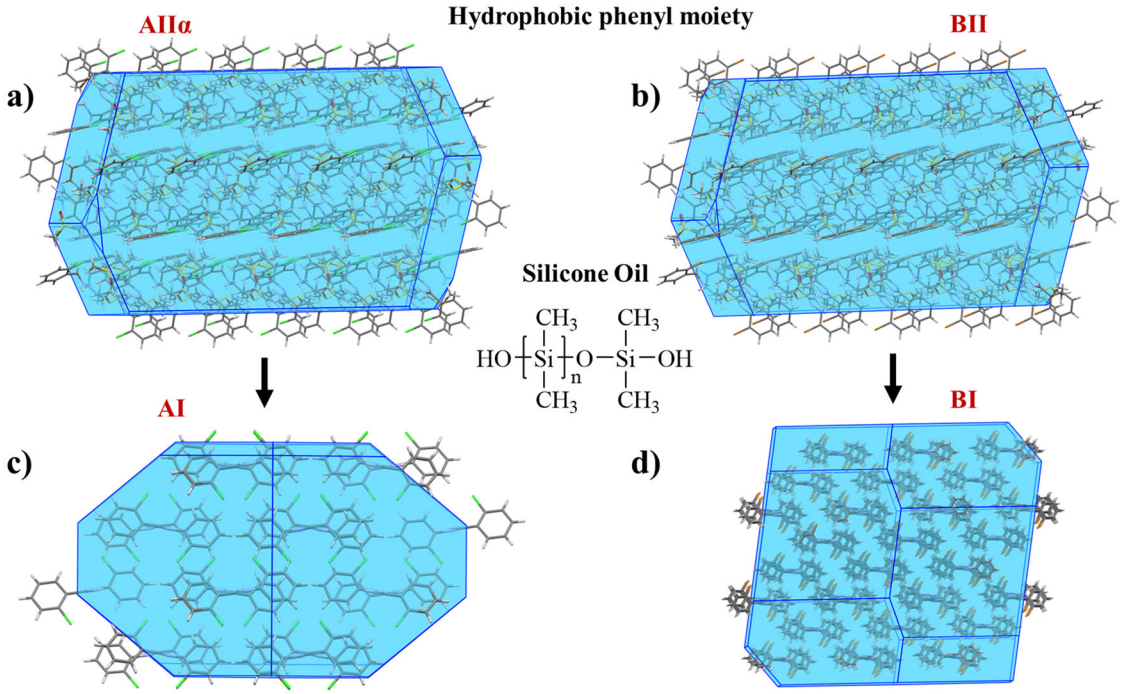

Fig. 12 | Crystal morphology. BFDH morphology of **a AIIα**, and **b BII** and their respective phase transition to **c AI**, and **d BI**, when immersed in SO.

BFDH morphology analysis indicates that hydrophobic regions of the molecular fragments, particularly the phenyl rings and the hydrophobic portions of the DMSO (represented as magenta) solvent, are exposed on the crystal surface (Fig. 11a, b). These interact with SO, destabilizing weakly attached surface molecules and initiating molecular movement. This activity triggers a phase transition at the crystal surface of **AIIα** and **BII**, subsequently leading to nucleation and growth of the **AI** and **BI** phases, respectively (Fig. 11c, d). The phase transition is evident in the morphological change from block to needle in both solvatomorph crystals. Due to their isomorphous nature, the rate of phase transition remains nearly uniform. Additionally, lattice energy calculations confirm that **AI** and **BI** form has greater stability compared to **AIIα** and **BII**, with this energy difference likely being the primary driver of the observed SCSC phase transition (Supplementary Table 15).

Conclusions

The polymorphic forms of **A** (**AIIα** and **AI**) and **B** (**BII** and **BI**) emerge when crystallized from different solvents. When both compounds are crystallized in DMSO at ambient temperature, they exhibit isomorphous crystal structures **AIIα** and **BII**. Notably, a martensitic phase transition occurs between **AIIα** ↔ **AIIβ**, driven by complete rotational disorder of the DMSO molecules. This order-disorder transition, accompanied by twinning, was investigated using variable-temperature SCXRD, which also confirmed its reversible nature. *Xpac* analysis revealed no change in the overall crystal structures, reinforcing the conclusion that the DMSO solvent mediates this order-disorder transition. Crystal packing analysis highlights the presence of strong tetrameric assemblies. Variable-temperature SCXRD highlights the dynamic behavior of DMSO during the **AIIα** ↔ **AIIβ** phase transition. In the **AII** system, the crystal lattice accommodates the rotational disorder of DMSO molecules, primarily due to Cl…Cl interactions that bridge the tetramers. In contrast, **BII** does not exhibit such a transition; the presence of strong Br…Br interactions restricts the available space in the lattice, restricting the DMSO reorientation. A distinct phase transition is observed when single crystals of **AIIα** and **BII** are immersed in SO, transforming into **AI** and **BI**, respectively. This transformation follows a *nucleation and growth mechanism*, where the daughter phase (**AI** and **BI**) originates from the parent crystals (**AIIα** and **BII**). Thermal characterization, including repeated DSC thermograms, along with TGA and HSM experiments, confirms the formation of the more thermodynamically stable **AI** and **BI** forms. Lattice energy calculations further support this, revealing more negative energy values for **AI** and **BI**, compared to **AIIα** and **BII**, indicating greater stability. Additionally, BFDH morphology analysis shows the presence of hydrophobic groups on the crystal surfaces, which promote interaction with SO and facilitate nucleation of **AI** and **BI**. *This study presents the first known instance in which a solvent plays a dual role, facilitating a temperature-driven martensitic phase transition and initiating a nucleation and growth mechanism via external chemical stimulus (SO).* These findings highlight the critical influence of solvent molecules on polymorphic behavior and phase stability.

Methods

Materials

All the reactants and solvents used were purchased from Sigma Aldrich and used without further purification. Crystallization solvents, especially of HPLC grade, were also sourced from Sigma Aldrich and employed as received.

Synthesis

A mixture of anhydrous $AlCl_3$ (1.2 eq) and halogenated benzonitrile (1.0 eq) was heated in an oil bath at 100 °C until a homogeneous melt formed. Halogenated aniline (1.0 eq) was then added dropwise, and the reaction was stirred at 120 °C for 6 h under dry conditions using a $CaCO_3$ guard tube. Progress was monitored by TLC. The resulting black solid was extracted with NaOH solution and dichloromethane, washed with water, dried over Na_2SO_4, and purified by column chromatography to afford the desired product.

Thermogravimetric analysis (TGA)

Thermogravimetric analysis (TGA) of solvatomorph crystals **AIIα** and **BII** was performed using a Perkin-Elmer TGA 8000 with 10 mg of sample. The analysis provided a thermal profile correlating sample weight percentage with temperature (°C), allowing dedication of hydrates and volatile components.

Single-crystal X-ray diffraction (SCXRD)

Single-crystal data for the polymeric forms of crystals **A** and **B** were collected on Bruker D8 VENTURE and D8 Quest diffractometers equipped with the PHOTON III system. Measurements employed an Oxford cryostream for low-temperature control with monochromatic Mo Kα (λ = 0.71073 Å) and Cu Kα (λ = 1.5406 Å) radiation. Data collection, unit cell measurements, integration, scaling, and absorption correction (multi-scan using SADABS[51]) were conducted for all datasets, except **AIIβ**, which was processed using TWINABS[52] with Bruker APEX 5[53]. Structures refinement was carried out by a full-matrix least-squares approach in SHELXL[54], integrated into the Olex2[55] suite. Non-hydrogen atoms were refined anisotropically; heteroatomic hydrogens were located via difference Fourier maps, while others were placed geometrically using a riding model and refined isotropically. Crystal packing was analyzed with Mercury[56], and geometrical calculations were performed using PARST[57] and PLATON[58].

AIIα undergoes non-merohedral twinning during an enantiotropic SCSC phase transition to **AIIβ** at temperatures equal to or below 198 K. Twinning corresponds to a 180 ° rotation about the *b*-axis in a *non-standard* triclinic configuration aligned with the monoclinic *b*-axis, confirmed by precession images over the 0kl plane down to 100 K.

Variable-temperature unit cell data

Unit cell determination for **AIIα** and **BII** single crystals was performed on a Bruker Quest diffractometer with a PHOTON III detector using Mo Kα radiation. Phi-scans were recorded between 298 K to 110 K in 10 K intervals, with cooling and heating controlled at 1 K per minute via an Oxford Cryostream. Data collection and integration were carried out using APEX5 software.

Differential scanning calorimetry (DSC)

DSC was performed on a Perkin-Elmer DSC 6000 from 25 °C to 200 °C under nitrogen, using bulk powder and polymorphs of **A** and **B** at a scan rate of 1 and 5 °C min^{-1}. Samples were sealed in covered aluminum pans, and heat flow was recorded as a function of temperature. Low-temperature DSC was carried out on a NETZSCH 3500 Sirius, scanning from 30 °C to −170 °C with liquid nitrogen cooling and a nitrogen purge of 20 mlmin-1. A 19 mg sample was cycled at 1 Kmin-1 with a 2-min isothermal hold at 170 °C and 30 °C.

Hot stage microscopy (HSM)

HSM was performed on suitable single crystals of both solvatomorphs using a Linkam LTS420 equipment coupled to a Leica polarizing microscope. Heating was applied from 20 to 200 °C at a constant rate of 1 °C min^{-1}.

Crystal Explorer

Energy framework analysis was carried out using *Crystal Explorer*[59] to visualize intermolecular interactions in the crystal structures. Computations were based on .cif files, with hydrogen atoms normalized from neutron diffraction data. A 3.8 Å cluster radius was applied and complete the remaining fragments of molecules. Interaction energies were calculated using the CE-B3LYP method with the 6-31G (d, p) basis set. Results are shown as cylindrical tubes representing the 3D interaction topology.

Crystal morphology predictions

These predictions were performed for the two phases, namely, **AIIα** and **BII** were performed using the Materials Studio[50] (version 6.1) software with the "Fine" setting, applying the universal force field. Atomic charges for the calculations were determined using the charge equilibrium (QEq) method.

Data availability

All variable-temperature SCXRD data and the X-ray crystallographic coordinates for the structure described in this study have been deposited at the Cambridge Crystallographic Data Centre (CCDC) under the deposition numbers 2243616, 2243610, 2452264, 2452265, 2452266, 2452267, 2452268, 2452269, 2452270, 2452271. These data are freely accessible through the CCDC website https://www.ccdc.cam.ac.uk/structures. The supplementary materials include additional details on the synthesis, as well as the corresponding NMR, TGA, DSC analyses, and theoretical calculations such as XPac, energy framework analysis, and lattice energy calculations.

Received: 4 June 2025; Accepted: 17 September 2025;
Published online: 05 November 2025

References

1. Bernstein, J. *Polymorphism in Molecular Crystals* (Oxford University Press, 2020).
2. Steiner, T. The hydrogen bond in the solid state. *Angew. Chem. Int. Ed. Engl.* **41**, 48–76 (2002).
3. Martinez, C. R. & Iverson, B. L. Rethinking the term "pi-stacking. *Chem. Sci.* **3**, 2191 (2012).
4. Zou, K. et al. Solvent-induced reversible high-temperature phase transition in crown ether clathrates. *New. J. Chem.* **46**, 8232–8238 (2022).
5. Bhandary, S. & Chopra, D. Observation of rapid desolvation of hexafluorobenzene involving single-crystal-to-single-crystal phase transition in a nonporous organic host. *Cryst. Growth Des.* **18**, 27–31 (2018).
6. Aakeroy, C. B. & Seddon, K. R. The hydrogen bond and crystal engineering. *Chem. Soc. Rev.* **22**, 397–407 (1993).
7. Desiraju, G. R. Supramolecular synthons in crystal engineering—a new organic synthesis. *Angew. Chem. Int. Ed. Engl.* **34**, 2311–2327 (1995).
8. Li, R., Hu, W., Liu, Y. & Zhu, D. Micro- and nanocrystals of organic semiconductors. *Acc. Chem. Res.* **43**, 529–540 (2010).
9. Park, S. K., Kim, J. H. & Park, S. Y. Organic 2D optoelectronic crystals: charge transport, emerging functions, and their design perspective. *Adv. Mater.* **30**, 1704759 (2018).
10. Biradha, K. & Santra, R. Crystal engineering of topochemical solid state reactions. *Chem. Soc. Rev.* **42**, 950–967 (2013).
11. Sutton, C., Risko, C. & Brédas, J.-L. Noncovalent intermolecular interactions in organic electronic materials: implications for the molecular packing vs electronic properties of acenes. *Chem. Mater.* **28**, 3–16 (2016).
12. Park, S. K. et al. Super- and ferroelastic organic semiconductors for ultraflexible single-crystal electronics. *Angew. Chem. Int. Ed. Engl.* **59**, 13004–13012 (2020).
13. Ahmed, E., Karothu, D. P. & Naumov, P. Crystal adaptronics: mechanically reconfigurable elastic and superelastic molecular crystals. *Angew. Chem. Int. Ed. Engl.* **57**, 8837–8846 (2018).
14. Herbstein, F. H. On the mechanism of some first-order enantiotropic solid-state phase transitions: from Simon through Ubbelohde to Mnyukh. *Acta Crystallogr. B Struct. Sci.* **62**, 341–383 (2006).
15. Dunitz, J. D. Phase transitions in molecular crystals from a chemical viewpoint. *Pure Appl. Chem.* **63**, 177–185 (1991).
16. Christian, J. W., Olson, G. B. & Cohen, M. Classification of displacive transformations: what is a martensitic transformation? *J. Phys. IV Fr.* **5**, C8–C10 (1995).
17. Mnyukh, Y. *Fundamentals of Solid-State Phase Transitions, Ferromagnetism and Ferroelectricity* (Bloomington, 2009).
18. Takamizawa, S. & Takasaki, Y. Shape-memory effect in an organosuperelastic crystal. *Chem. Sci.* **7**, 1527–1534 (2016).
19. Takamizawa, S. & Takasaki, Y. Superelastic shape recovery of mechanically twinned 3,5-difluorobenzoic acid crystals. *Angew. Chem. Int. Ed. Engl.* **54**, 4815–4817 (2015).
20. Takamizawa, S. & Miyamoto, Y. Superelastic organic crystals. *Angew. Chem. Int. Ed. Engl.* **53**, 6970–6973 (2014).
21. Karothu, D. P., Weston, J., Desta, I. T. & Naumov, P. Shape-memory and self-healing effects in mechanosalient molecular crystals. *J. Am. Chem. Soc.* **138**, 13298–13306 (2016).

22. Nath, N. K. et al. Single-crystal-to-single-crystal transition in an enantiopure [7]helquat salt: the first observation of a reversible phase transition in a helicene-like compound. *Chemistry* **21**, 13508–13512 (2015).
23. Hasija, A. et al. Tracing shape memory effect and elastic bending in a conformationally flexible organic salt. *J. Mater. Chem. C* **10**, 4257–4267 (2022).
24. Panda, M. K. et al. Colossal positive and negative thermal expansion and thermosalient effect in a pentamorphic organometallic martensite. *Nat. Commun.* **5**, 4811 (2014).
25. Yao, Z.-S. et al. Molecular motor-driven abrupt anisotropic shape change in a single crystal of a Ni complex. *Nat. Chem.* **6**, 1079–1083 (2014).
26. Tamboli, M. I., Karothu, D. P., Shashidhar, M. S., Gonnade, R. G. & Naumov, P. Effect of crystal packing on the thermosalient effect of the pincer-type diester naphthalene-2,3-diyl-bis(4-fluorobenzoate): a new class II thermosalient solid. *Chemistry* **24**, 4133–4139 (2018).
27. Vogelsberg, C. S. & Garcia-Garibay, M. A. Crystalline molecular machines: function, phase order, dimensionality, and composition. *Chem. Soc. Rev.* **41**, 1892–1910 (2012).
28. Colin-Molina, A. et al. Thermosalient amphidynamic molecular machines: motion at the molecular and macroscopic scales. *Matter* **1**, 1033–1046 (2019).
29. Davey, R. J. et al. Stabilization of a metastable crystalline phase by twinning. *Nature* **366**, 248–250 (1993).
30. Simões, R. G. et al. Polymorphism in simvastatin: twinning, disorder, and enantiotropic phase transitions. *Mol. Pharm.* **15**, 5349–5360 (2018).
31. Kaftory, M., Botoshansky, M., Kapon, M. & Shteiman, V. Irreversible single-crystal to polycrystal and reversible single-crystal to single-crystal phase transformations in cyanurates. *Acta Crystallogr. B* **57**, 791–799 (2001).
32. Wang, K., Wang, C., Mishra, M. K., Young, V. G. & Sun, C. C. Reversible facile single-crystal-to-single-crystal polymorphic transition accompanied by unit cell volume expansion and twinning. *CrystEngComm* **23**, 2648–2653 (2021).
33. Cruz-Cabeza, A. J., Day, G. M. & Jones, W. Structure prediction, disorder and dynamics in a DMSO solvate of carbamazepine. *Phys. Chem. Chem. Phys.* **13**, 12808–12816 (2011).
34. Lynch, V. M., Gale, P. A., Sessler, J. L. & Madeiros, D. Room-temperature monoclinic and low-temperature triclinic phase-transition structures of *meso*-octamethylcalix[4]pyrrole–dimethyl sulfoxide (1/1). *Acta Crystallogr. C Cryst. Struct. Commun.* **57**, 1426–1428 (2001).
35. Dey, D. & Chopra, D. N–H···π induced configurational isomerism and the role of temperature in the Z to E isomerization of 2-fluoro-N′-(3-fluorophenyl)benzimidamide. *CrystEngComm* **17**, 5288–5298 (2015).
36. Dey, D. & Chopra, D. Solvatomorphism in (Z)-4-fluoro-N′-(3-fluorophenyl)benzimidamide: the role of intermolecular O–H···F interaction. *CrystEngComm* **18**, 8291–8300 (2016).
37. Bhandary, S. & Chopra, D. Silicone oil induced spontaneous single-crystal-to-single-crystal phase transitions in ethynyl substituted ortho- and meta-fluorinated benzamides. *Cryst. Growth Des.* **17**, 4533–4540 (2017).
38. Meenan, P. Crystal morphology predictive techniques to characterize crystal habit: application to aspirin ($C_9H_8O_4$). *Sep. Purif. Crystal.* **667**, 2–17 (1997).
39. Groom, C. R., Bruno, I. J., Lightfoot, M. P. & Ward, S. C. The Cambridge Structural Database. *Acta Crystallogr. B* **72**, 171–179 (2016).
40. Kálmán, A., Párkányi, L. & Argay, G. Classification of the isostructurality of organic molecules in the crystalline state. *Acta Crystallogr. B* **49**, 1039–1049 (1993).
41. Gelbrich, T. & Hursthouse, M. B. Systematic investigation of the relationships between 25 crystal structures containing the carbamazepine molecule or a close analogue: a case study of the XPac method. *CrystEngComm* **8**, 448–460 (2006).
42. Gelbrich, T. & Hursthouse, M. B. A versatile procedure for the identification, description and quantification of structural similarity in molecular crystals. *CrystEngComm* **7**, 324 (2005).
43. Ranjan, S. et al. Isomorphism: 'molecular similarity to crystal structure similarity' in multicomponent forms of analgesic drugs tolfenamic and mefenamic acid. *IUCrJ* **7**, 173–183 (2020).
44. Gavezzotti, A. & Simonetta, M. Crystal chemistry in organic solids. *Chem. Rev.* **82**, 1–13 (1982).
45. Buergi, H. B. & Dunitz, J. D. From crystal statics to chemical dynamics. *Acc. Chem. Res.* **16**, 153–161 (1983).
46. Van Den Ende, J. A., Ensing, B. & Cuppen, H. M. Energy barriers and mechanisms in solid–solid polymorphic transitions exhibiting cooperative motion. *CrystEngComm* **18**, 4420 (2016).
47. Mittapalli, S., Perumalla, D. S., Nanubolu, J. B. & Nangia, A. Thermomechanical effect in molecular crystals: the role of halogen-bonding interactions. *IUCrJ* **4**, 812–823 (2017).
48. Saha, B. K., Veluthaparambath, R. V. P. & Krishna, G. V. Halogen···halogen interactions: nature, directionality and applications. *Chemistry* **18**, e202300067 (2023).
49. Shruti, I. & Thakur, T. S. A mechanochemical route for the synthesis of diphenyleneiodonium salts and the estimation of their relative solid-state reactivities. *Chem. Methods* **5**, e2500002 (2025).
50. Accelrys Software Inc. Materials Studio, version 6.1 (Accelrys Inc., 2012).
51. Krause, L., Herbst-Irmer, R., Sheldrick, G. M. & Stalke, D. Comparison of silver and molybdenum microfocus X-ray sources for single-crystal structure determination. *J. Appl. Cryst.* **48**, 3–10 (2015).
52. TWINABS v.2012/1 (Bruker AXS Inc., 2012).
53. Bruker APEX v.5 (Bruker AXS Inc., 2023).
54. Sheldrick, G. M. A short history of *SHELX*. *Acta Crystallogr. A Found. Crystallogr.* **64**, 112–122 (2008).
55. Dolomanov, O. V., Bourhis, L. J., Gildea, R. J., Howard, J. A. K. & Puschmann, H. OLEX2: a complete structure solution, refinement and analysis program. *J. Appl. Crystallogr.* **42**, 339–341 (2009).
56. Macrae, C. F. et al. *Mercury 4.0*: from visualization to analysis, design and prediction. *J. Appl. Crystallogr.* **53**, 226–235 (2020).
57. Nardelli, M. PARST95—an update to PARST: a system of Fortran routines for calculating molecular structure parameters from the results of crystal structure analyses. *J. Appl. Crystallogr.* **28**, 659–659 (1995).
58. Spek, A. L. Single-crystal structure validation with the program *PLATON*. *J. Appl. Crystallogr.* **36**, 7–13 (2003).
59. Spackman, P. R. et al. *CrystalExplorer*: a program for Hirshfeld surface analysis, visualization and quantitative analysis of molecular crystals. *J. Appl. Crystallogr.* **54**, 1006–1011 (2021).

Acknowledgements

S.S., S.D., P.G. and D.C. acknowledge IISER Bhopal for providing access to the central instrumentation facility (CIF), including SCXRD, PXRD, DSC, TGA, HSM, and related infrastructure. S.S. expresses gratitude to UGC for the Senior Research Fellowship, while A.G. acknowledges support from the DST Inspire fellowship. A.G. and S.M. also thank CSIR-CGCRI for granting access to the low-temperature DSC facility.

Author contributions

The project was conceptualized by D.C., including data analysis, interpretation, and scientific inputs on the design of experiments. The synthesis was carried out by P.G. and S.S. Crystallizations and all the phase transition experiments were performed by S.S., while S.D. contributed toward the understanding of the order-disorder phase transition and developing the data collection strategies for single-crystal data collection. A.G. and S.M. conducted the low-temperature DSC experiments. The manuscript was written by S.S., with inputs from all the authors.

Competing interests
The authors declare no competing interests.

Additional information
Supplementary information The online version contains supplementary material available at https://doi.org/10.1038/s42004-025-01715-8.

Correspondence and requests for materials should be addressed to Deepak Chopra.

Peer review information *Communications Chemistry* thanks Leonardo Lo Presti and the other anonymous reviewers for their contribution to the peer review of this work.